ultrasonic actuators with optical encoder (rated torque 50mNm, custom order, Fukoku, Japan) because of various advantages of ultrasonic motor; compact size and light weight for miniaturization, high holding torque, clean environment for future clinical application, and suitable for hollow-shaft configuration. We use a couple of friction wheels with opposite tilting angle. They provide symmetrical spiral motions like right-handed and left-handed screws, and they are combined to generate rotation and translation (Fig. 4).

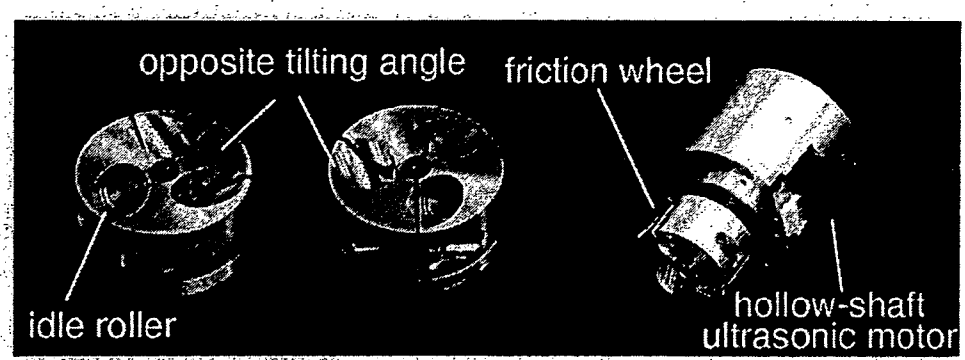

Figure 3. A couple of friction wheel; Each friction wheel has three tilted driving rollers with opposite tilting angle (left). Hollow-shaft ultrasonic motor is adopted for actuation (right)

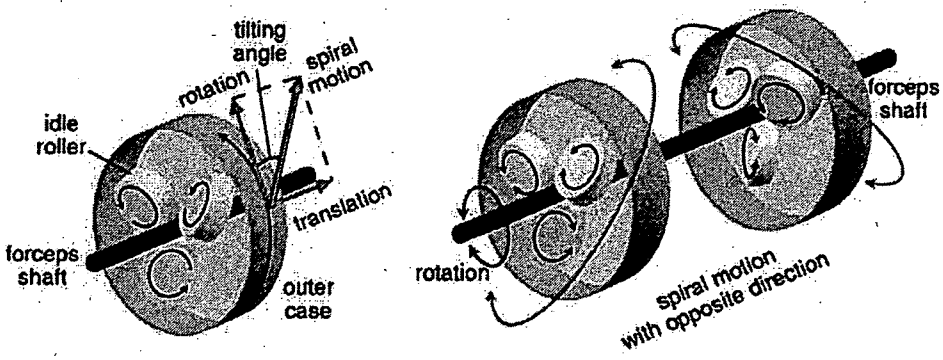

Figure 4. Friction wheel mechanism; friction wheel travels spirally around the forceps shaft (left). Opposite tilting angle generates two different spiral shapes like right-handed and left-handed screws (right)

For the axial rotation of forceps shaft, two friction wheels are rotated in the same direction. In that case, driving rollers and shaft does not have relative speed, so that spiral motions are not generated and forceps shaft rotates at the same speed of friction wheel. For the longitudinal translation, two friction wheels are rotated in the opposite direction. In this case, spiral motions are generated. The rotational components of spiral motion are cancelled mutually and remaining translation drives the forceps (Fig. 5).
The mechanism to generate translation can be shown using mathematical expression (Fig. 6).

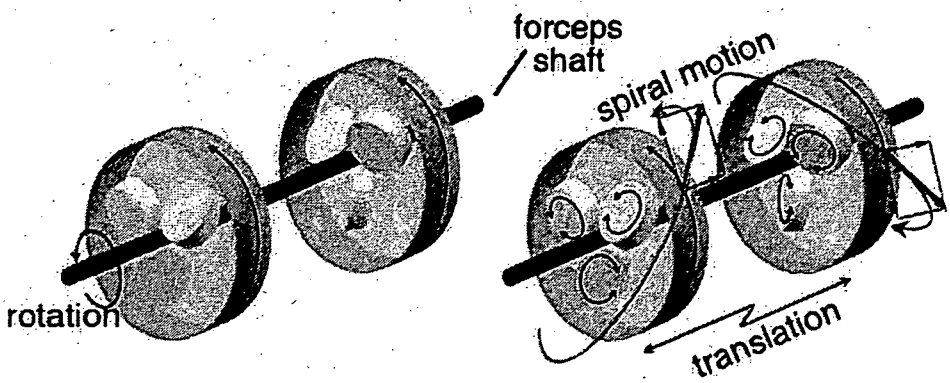

Figure 5. Driving principle of friction wheel mechanism: Rotational motion is generated by rotating both motors in the same direction (left). When each motor is driven in the opposite direction, rotational motions are cancelled mutually and remaining translational motion drives forceps in the longitudinal direction (right)

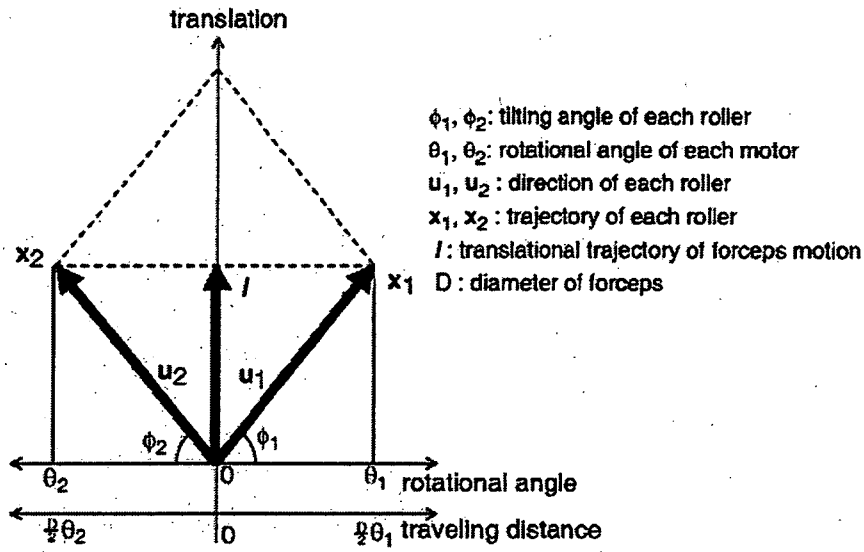

Figure 6. Translational motion can be shown by expanding the surface of forceps to a plane Here, each roller has tilting angle of ϕ_1 and ϕ_2. When outer cases are rotated by θ_1 and θ_2, trajectory of each roller is as follows;

$$\begin{cases} x_1 = \frac{D}{2}\theta_1 u_1 = \frac{1}{2}\begin{bmatrix} D\theta_1 \\ D\theta_1 \tan(\phi_1) \end{bmatrix} \\ x_2 = \frac{D}{2}\theta_2 u_2 = \frac{1}{2}\begin{bmatrix} D\theta_2 \\ D\theta_2 \tan(\phi_2) \end{bmatrix} \end{cases} \quad (1)$$

As the traveling distance is written as the average of two friction wheels, translation can be express using rotational angle of each motor (θ_1 and θ_2) and tilting angle (ϕ_1 and ϕ_2);

$$
\begin{aligned}
l &= \frac{x_1 - x_2}{2} \\
&= \begin{bmatrix} \frac{D}{4}(\theta_1 - \theta_2) \\ \frac{D}{4}(\theta_1 \tan(\phi_1) + \theta_2 \tan(\phi_2)) \end{bmatrix} \\
&= \begin{bmatrix} \frac{D}{4}(\theta_1 - \theta_2) \\ \frac{D}{4}(\theta_1 + \theta_2)\tan(\frac{\pi}{6}) \end{bmatrix} \qquad \left(\phi_1 = \phi_2 = \frac{\pi}{6}\right) \\
&= \begin{bmatrix} 0 \\ \frac{D}{2}\theta \tan(\frac{\pi}{6}) \end{bmatrix} \qquad (\theta_1 = \theta_2 = \theta)
\end{aligned} \tag{2}
$$

Here, we used 30 deg ($\pi/6$ rad) for tilting angle of rollers and θ for rotational angle of each motor. As shown in eq. (2), the translational distance is controlled by the rotational angle of actuator like a ball screw.

This mechanism is proposed by Vollenweider for surgery simulator (Vollenweider, et al, 1998). Ikuta, et al. also adopted the similar mechanism for axial rotation and longitudinal translation of colonoscope in the virtual endoscope training system (Ikuta, et al., 1998). To the best of authors' knowledge, this is the first prototype that uses this kind of rotation and translation mechanism not for simulator but for real manipulator.

2.3 Gimbals mechanism

Gimbals mechanism has two mutually-perpendicular intersectional rotational axes and realizes pivoting motion of forceps with wide working range around the trocar port. The simple kinematics eases numerical control.

A concern about the location of rotational centre of the mechanism should be discussed. Many studies have proposed the necessity of the remote centre of motion (RCM) mechanism to realize pivot motion with no mechanical part at the trocar port; such as R-guide (Mitsuishi, et al., 2003) and parallel-linkage mechanism (Taylor, et al., 1995, Madhani, et al., 1998, and Kobayashi, et al., 2002). As gimbals mechanism has its rotational centre inside it, not at the incision hole, the rotational centre is located above trocar port and forceps pulls abdominal wall accompanying its pivot motion. As we reported in the past publication (Suzuki, et al., 2002), the result of preliminary in-vivo experiment using pig showed no problem; such as expansion of incision hole and bleeding. We conclude that gimbals mechanism will not damage the abdominal wall because abdominal muscle got relaxed under anaesthesia and incision hole follows the motion of forceps, although the required torque increased to pull the abdominal wall according to the pivot motion of forceps and actuators should be carefully selected. We adopted DC servomotor (ENC-185801, CITIZEN CHIBA PRECISION Co., LTD) to control each rotational axis.

3. Evaluation

3.1 Separation between translation and rotation

One of advantages of FWM is that it realizes rotation and translation with one miniaturized mechanism. For appropriate rotation and translation, we need two conditions; one is the shape of each spiral and the other is rotational speed of each motor. In other words, the lead length of each spiral motion generated by friction wheel should be the same, and rotational speed of each motor should be the same. This is because rotational component of spiral motion must be the same to be cancelled mutually. Our former studies, however, showed that the friction wheel mechanism provided rotational error in translation. We measured the rotational error when 90 mm translation, equivalent to 1800 deg rotation of actuator, was input. The rotating angle of each actuator was controlled using pulse signal from rotary encoders mounted on the motor. The rotating angle of forceps shaft was measured using digital microscope (VH-7000C, Keyence, Japan) with 0.5 deg resolution. The result of error evaluation is shown in Table. 1 (Suzuki, et al., 2005). Measured error was large compared to the required specification we set for this manipulator.

input	error factor	required spec.	average +/- S.D.
translation (90 mm, 1800 deg)	rotation	less than1 deg	14.5 +/- 3.0 deg

Table 1. Rotational error of friction wheel mechanism in translational input

3.2 Error analysis based on mechanical error

For the error correction, we analyze the cause of rotational error in translational motion. As mentioned above, the error motion is caused by different spiral shape generated by each friction roller and/or different rotating angle of each actuator. As we control the actuators using rotary encoders, we can omit the possibility of different rotating angle. Thus, the cause of unstable motion is mismatch of lead length between each friction roller. Lead length error is caused by tilting angle error of the friction rollers. The angle error is determined by the machining error in prototyping process.

We discussed the cause of rotational error in translation and its correction method based on the mechanism of friction wheel. Error analysis is shown here using Fig. 7.

Rotational error is shown as follows;

$$\Delta\theta=\frac{1}{2}(\hat{\theta}_1-\hat{\theta}_2) \tag{3}$$

Because the forceps shaft is rigid, the translational distance generated by each roller is the same, and sum of rotational angle are the same between each roller.

$$\begin{cases} \hat{\theta}_1\tan(\phi+\Delta\phi_1) &= \hat{\theta}_2\tan(\phi+\Delta\phi_2) \\ \hat{\theta}_1+\hat{\theta}_2 &= \theta_1+\theta_2 \end{cases} \tag{4}$$

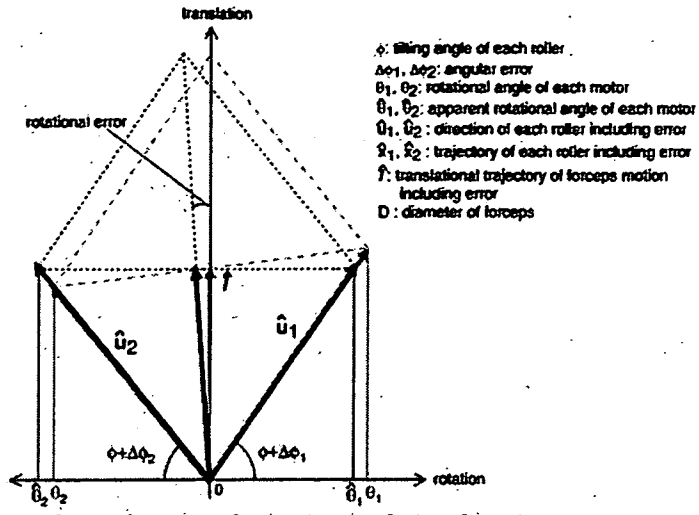

Figure 7. Error analysis of rotational error in translational motion

When these simultaneous equations (4) are solved for $\hat{\theta}_1$ and $\hat{\theta}_2$, they are shown as follows;

$$\begin{cases} \hat{\theta}_1 = \dfrac{\tan(\phi+\Delta\phi_2)}{\tan(\phi+\Delta\phi_1)+\tan(\phi+\Delta\phi_2)}(\theta_1+\theta_2) \\ \hat{\theta}_2 = \dfrac{\tan(\phi+\Delta\phi_1)}{\tan(\phi+\Delta\phi_1)+\tan(\phi+\Delta\phi_2)}(\theta_1+\theta_2) \end{cases} \tag{5}$$

Consequently, $\Delta\theta$ (eq. (3)) is shown using eq.(5).

$$\begin{aligned} \Delta\theta &= \frac{1}{2}(\hat{\theta}_1-\hat{\theta}_2) \\ &= -\frac{1}{2}\frac{\tan(\phi+\Delta\phi_1)-\tan(\phi+\Delta\phi_2)}{\tan(\phi+\Delta\phi_1)+\tan(\phi+\Delta\phi_2)}(\theta_1+\theta_2) \end{aligned} \tag{6}$$

This means that the rotational error is proportional to the sum of input rotating angle (θ_1, θ_2), and that the coefficient is determined using only mechanical error of tilting angle ($\Delta\phi_1$ and $\Delta\phi_2$), thus the error could be compensated using correction factor. On the assumption that rotational error of $\Delta\theta$ is observed when angle of θ_0 is input to generate translation, the correction factor is analyzed. As the condition, we have following equations. Equation (7) means the translational distance is expressed in two ways. The first equation in eq.(8) means input angle for each driving roller is the same in the case of translational input, and other equations are geometrically trivial.

$$\hat{\theta}_1\tan(\phi+\Delta\phi_1)=\frac{1}{2}\left(\theta_1\tan(\phi+\Delta\phi_1)+\theta_2\tan(\phi+\Delta\phi_2)\right) \tag{7}$$

$$\begin{cases} \theta_1 = \theta_2 &= \theta_0 \\ \tan(\phi+\Delta\phi_1) &= \dfrac{\hat{l}}{\hat{\theta}_1} \\ \tan(\phi+\Delta\phi_2) &= \dfrac{\hat{l}}{\hat{\theta}_2} \end{cases} \tag{8}$$

When equations (8) are assigned to eq.(6) and (7), $\hat{\theta}_1/\theta_0$ and $\hat{\theta}_2/\theta_0$ are shown as eq.(9).

$$\begin{cases} \dfrac{\hat{\theta}_1}{\theta_0} &= \dfrac{-2k+1+\sqrt{4k^2+1}}{2} \\ \dfrac{\hat{\theta}_2}{\theta_0} &= \dfrac{2k+1+\sqrt{4k^2+1}}{2} \\ & \left(k=\Delta\theta/\theta_0\right) \end{cases} \Rightarrow \begin{cases} \dfrac{\hat{\theta}_1}{\theta_0} &= 1-k \\ \dfrac{\hat{\theta}_2}{\theta_0} &= 1+k \\ & (k \ll 1) \end{cases} \tag{9}$$

As they are the error coefficient of driving rollers, the inverse of those coefficients are the correction factor C_1 and C_2 (eq.(10)).

$$\begin{cases} C_1 &= \dfrac{\theta_0}{\hat{\theta}_1} = \dfrac{1}{1-k} = 1+k \\ C_2 &= \dfrac{\theta_0}{\hat{\theta}_2} = \dfrac{1}{1+k} = 1-k \\ & (k \ll 1) \end{cases} \tag{10}$$

Consequently, the correction factor can be expressed using k that is determined by input angle ($\Delta\theta$) and measured error angle (θ_0).

3.3 Re-evaluation of separation after compensation

We measured rotational error again. In this measurement, we applied the correction factor k by assigning 1800 deg to θ_0 and 14.5 deg to $\Delta\theta$. Result is shown in Table 2 comparing the result of the case without correction factor. The rotational error was reduced more than 90 % by the error correction factor (Suzuki, et al., 2005).

input	error factor	correction factor	average +/- S.D (deg)
translation (90 mm, 1800 deg)	rotation	without	14.5 +/- 3.0
		with	1.0 +/- 1.0

Table 2. Rotational error of friction wheel mechanism in translational input with/without correction factor

4. Discussion

For realization of stable forceps manipulation using friction wheel mechanism, we analyzed the mechanical configuration of manipulator and proposed a correcting factor based on the input rotating angle and measured rotational error, so that the error was reduced by 90%. When the 90 mm translation is input, the error was approximately 1.0 deg. In laparoscopic surgery, innermost target is sometimes located 300 mm from incision hole. In that case, the rotational error will increase up to approximately 3.0 deg. As it does not meet the required specification of 1deg accuracy, we have to find other causes of unstable motion.

One of possible causes is the variation of correction factor. We calculated the correction factor as a constant value from limited number of sets of measured error and input rotating angle. The error correction factor may change depending on the surface condition of forceps shaft, so we need to change correction factor dynamically. Another cause is slip between friction rollers and forceps shaft. In the current prototype, the forceps position is calculated from encoder value and controlled in semi-closed feedback loop. We do not consider position error caused by slight slip or its accompanying accumulated error.

These issues could be solved by closed feedback control loop using direct sensing of forceps position. As implementation methods, we can use three dimensional optical position sensor and/or texture recognition system like optical mouse.

5. Conclusion

In this study, we introduce a compact forceps manipulator with four DOFs for laparoscopic surgery. It consists of two mechanical parts; friction wheel mechanism and gimbals mechanism. Friction wheel mechanism is space-saving and realizes two degrees of freedom of rotation and translation using a couple of friction wheel. Gimbals mechanism realizes wide working range and easy control. One of the drawbacks of FWM, rotational motion error in translational input, was shown and analyzed mathematically based on the mechanical configuration of manipulator. Rotational error was reduced more than 90 % by the error correction factor calculated from the mathematical analysis of mechanical configuration.

In the future works, we will work to modify mechanical configuration based on the results of this study and improve control method from semi-closed feedback control using rotary encoders to closed feedback control using direct position sensing method, such as three-dimensional optical position sensor. As another future work, we will integrate this forceps manipulator with robotized forceps, such as laser coagulator forceps with CCD camera (Suzuki, et al., 2004).

6. Acknowledgement

This work is partly supported by following grants;
-"Research for the Future Program (JSPS-RFTF 99I00904)" funded by Japan Society for the Promotion of Science
-Electro-Mechanic Technology Advancing Foundation
-"Research and Development of the Compact Surgical Robot System for Future Medical Care" funded by New Energy and Industrial Technology Development Organization (NEDO)

-"Research on medical devices for analyzing, supporting and substituting the function of human body" funded by Ministry of Health, Labour and Welfare
-JPSP(#18680041).

7. References

Ikuta, K. et al (1998). Virtual Endoscope System with Force Sensation. In :*Proceedings of the first international conference on medical image computing and computer-assisted intervention - MICCAI98, Lecture Note in Computer Science* 1496, pp.293-304, ISBN:3-540-65136-5, Cambridge, MA, USA, October, 1998, Springer.

Kobayashi, Y. et al (2002). Small Occupancy Robotic Mechanisms for Endoscopic Surgery. In : *Proceedings of the 5th international conference on medical image computing and computer assisted intervention* (MICCAI2002), *Part 1, Lecture Note in Computer Science* 2488, ISBN:3-540-44225-1, Tokyo, Japan, September, 2002, Springer.

Madhani, A. et al (1998). The Black Falcon: a teleoperated surgical instrument for minimally invasive surgery. In : *Proceedings of IEEE/RSJ international conference on intelligent robots and systems - IROS1998, vol.2,* pp.936-944, Victoria, BC, Canada, 1998, October, IEEE.

Mitsuishi, M. et al (2003). Development of a remote minimally-invasive surgical system with operational environment transmission capability. In :*Proceedings of the 2003 IEEE international conference on robotics and automation - ICRA2003,* pp. 2663-2670, Taipei, Taiwan, September, 2003, IEEE.

Suzuki, T. et al (2002). A new compact robot for manipulation forceps using friction wheel and gimbals mechanism. In : *Proceedings of the 16th international congress and exhibition computer-assisted radiology and surgery - CARS2002,* pp.314-319, ISBN:3-540-43655-3, Paris, France, 2002, June, Springer.

Suzuki, T. et al (2004). Development of a robotic laser surgical tool with an integrated video endoscope. In :*Proceedings of the 7th international conference on medical image computing and computer assisted intervention-MICCAI2004, Part II, Lecture Note in Computer Science* 3217, pp.25-32, ISBN:3-540-22977-9, Saint-Malo, France, September, 2004, Springer.

Suzuki, T. et al (2005). Compact forceps manipulator using friction wheel mechanism and gimbals mechanism for laparoscopic surgery. In :*Proceedings of the 8th international conference on medical image computing and computer assisted intervention-MICCAI2005, Part II, Lecture Note in Computer Science 3750,* pp.81-88, ISBN:978-3-540-29326-2, Palm Springs, CA, USA, October, 2005, Springer.

Taylor, RH. et al (1995). A telerobotic assistant for laparoscopic surgery. *IEEE Engineering in Medicine and Biology Magazine,* vol.14, no.9, May/Jun 1995, pp.279-288, ISSN:0739-5175.

Vollenweider, M. et al (1998). Surgery simulator with force feedback. In :*Proceedings of the 4th international conference on motion and vibration control - MOVIC98,* Zurich, Switzerland, 1998.

CHAPTER 7

METHODS IN COMBINED COMPRESSION AND ELONGATION OF LIVER TISSUE AND THEIR APPLICATION IN SURGICAL SIMULATION

ICHIRO SAKUMA
Department of Precision Engineering
School of Engineering, The University of Tokyo
7-3-1 Hongo Bunkyo-ku, Tokyo 113-8656, Japan
sakuma@miki.pe.u-tokyo.ac.jp

CHEEKONG CHUI
Institute of Environmental Studies
Graduate School of Frontier Sciences, University of Tokyo
7-3-1 Hongo Bunkyo-ku, Tokyo 113-8656, Japan
and
Department of Mechanical Engineering
National University of Singapore, E3-05-23 Engineering Drive 3
Singapore 119260, Singapore
mpecck@nus.edu.sg

A fundamental problem in computer aided surgical simulation is soft tissue modeling. It is difficult to represent the complex biomechanical properties and yet computational efficient for fast simulation. This paper reviews the methodologies for determination of the elastic properties of porcine liver tissues. The combined compression and elongation test is used as a unified framework to study the liver biomechanics for computer aided surgical simulation. At a length scale of approximately 10 mm, liver tissue is incompressible, anisotropic and nonlinear viscoelastic. It is stiffer during compression. The tissue sample will buckle under a mean stress of 2.313×10^5 Pa under compression. The Poisson's ratio was 0.466 ± 0.147 during compression and 0.431 ± 0.155 during elongation. Constitutive laws including strain energy based combined energy equation and equivalent stress and stain based multi-linear model were used in modeling the nonlinear stress-strain behavior of liver tissues under compression and elongation. Application of the experimental data and theoretical models is demonstrated via finite element simulation of liver organ deformation.

1. Introduction

Computer aided surgery (or computer integrated and robot assisted surgery) is performed to satisfy unmet complex needs in surgeries such as image guided surgeries. Image guided surgeries or minimally invasive surgeries are becoming increasingly popular. In an image guided surgery, the surgical procedure is facilitated by a real time correlation of the operative field to a monitor, which shows the

precise location of a selected surgical instrument to the surrounding structures. This is different from the conventional open surgery in which the surgeons can see the tissue being operated on directly. The image guided surgery is both beneficial to patients and cost-effective, and is fast becoming the standard of care for various surgeries.[1]

A computer aided surgery process is complex. In a typical process shown in Fig. 1, its components include preoperative imaging, modeling and segmentation, simulation, then registering sources of data and applying these to the intervention on the patient. The interventions are monitored, corrected, or extended, according to the results of intraoperative imaging. Virtual reality-based simulation of image guided surgery has been reported by various investigators. Virtual reality techniques[2] and the emergence of automatic surgical tools and robots[3] have been driving an exciting area of research–computer simulation of surgical procedures or computer aided surgical simulation.

Virtual reality and simulator-based technology systems have significant practical value in training and in evaluating user responses in situation-specific problem solving for both the military and industrial sectors.[4,5] It is only natural that this technology be utilized for medical applications. For example, the various surgical simulation systems for interventional radiology, cardiology and neuroradiology reported in Anderson *et al.*[6] and references cited therein focus on training of user skills, improving hand-eye coordination, training of specific patient management decision-making skills, training of very specific specialized skills, and evaluating treatment approaches for patient specific pretreatment planning. There are on-going research efforts to develop patient specific catheterization devices using simulation-based design technology.[7,8] Another application of computer programs enabling accurate modeling of soft tissue deformation is in surgical robot control systems for neurosurgery[9] as well as treatment of liver cancers.[10] Nevertheless, clinical applications of this surgical simulation technology are currently limited.

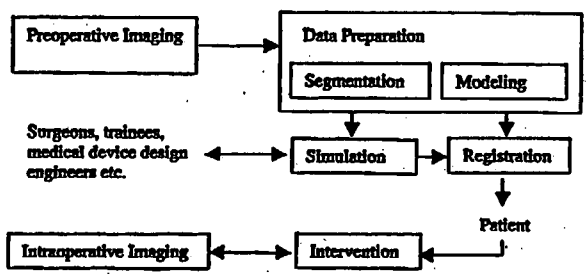

Fig. 1. Typical computer aided surgery process: The focus of this study is on surgical simulation, in particular the biomechanical modeling of liver tissue. Outcome of simulation may be used for training as well as medical device design and evaluation.

As of today, virtual reality is not likely to be found in the operating room.[11] The underlying computer-based anatomical models are not quite realistic enough. There should be a faithful representation of geometry, boundary and loading conditions as well as mechanical properties of the organ. The fundamental problem in anatomical modeling is the lack of "physics" in particular soft tissue modeling of liver, kidney and brain. It is desirable to have the behavior of the object depend on the constitutive properties of the object being simulated. The mechanical properties of liver, kidney and brain tissues are also different. Brain tissue is apparently softer and is more viscous compared to that of liver tissue. Several studies have underlined the importance of duly considering elastic tissue deformation.[12]

Precise information about the elastic properties and corresponding constitutive laws of biological soft tissues determines the performance of surgical simulators. These tissues are highly nonlinear and complex. Quantitative data about the biomechanical properties of soft tissues are few. It is a challenge to derive a representative constitutive law that is clinically relevant as well as computationally efficient for computer aided surgical systems. Basic research and measurement experiments are required to understand and model the biomechanics of soft tissue. The field of biomechanics which is defined as the research and analysis of the mechanics of living organisms places great emphasis on the physiological correctness of the mathematical model. On the other hand, computational efficiency is essential for practical clinical application. The approach employed here involves refining the conventional approaches based on continuum mechanics to measure and model the biomechanics of liver tissue for computer aided surgical simulation.

This paper is organized as follows. In Sec. 2, we discuss the various methods in measuring the mechanical properties of liver tissues with particular focus on the combined compression and elongation test. The combined compression and elongation test enabled zero stress state of the tissue sample to be precisely determined for the tensile test. In Sec. 3, we characterize the mechanical properties of liver tissue. When deformed, kidney and brain will behave differently from liver. It is necessary to have an in-depth investigation on the biomechanical properties of liver on its own. In Sec. 4, the strength and elastic modulus of liver tissues are investigated. Mathematical modeling of liver tissue mechanics is discussed in Sec. 5. It is more beneficial to model the stress–strain behavior from combined compression and elongation test than that of simply compression or simply elongation. Organ deformation involves both compressible and tensile displacement. Depending on the specific applications, the constitutive model used is a trade off between computational accuracy and interactivity. Section 6 describes biomechanical modeling of liver organ and surgical simulation of organ deformation. In surgical simulation, the biomechanical model has to be computationally efficient so that the computer simulation could provide a timely solution. Concludes Sec. 7 with a brief discussion on the future work.

2. Measurement of Liver Tissue Elasticity

The developments in computer aided surgery where precise information about the elastic properties of living tissues are desired fuels the recent interest and progress in measuring the mechanical properties of biological tissues. The emphasis of these measurement methods is on low speed loading condition.

Surgical instruments had been equipped with force-sensing capabilities allowing elasticity measurement during surgeries.[13,14] Pathak *et al.*[15] applied indentation methods for *in vivo* experiments on the skin. However, these techniques lacked well-defined boundary conditions during experiment and often failed to address the complex material properties of tissue with nonlinear constitutive equations. MR elastography[16] was a possible method for non-invasive imaging of elastic properties in non-homogeneous organs. This method spatially maps and quantifies small displacements caused by propagating harmonic mechanical waves. Nevertheless, the resulting very small displacements and frequency range could not predict the tissue behavior in the range of strains and strain rates observed during surgical interventions. Kauer *et al.*[17] presented a tissue aspiration method for *in vivo* determination of the material parameters of biological soft tissue. An explicit axisymmetric finite element simulation of the aspiration experiment is used together with a Levenberge-Marquardt algorithm to estimate the material model parameters in an inverse parameter determination process. This tissue aspiration method with inverse finite element characterization has well defined mechanical boundary conditions and could induce relatively large tissue deformation. However, the condition of axisymmetry assumed in this method could not be met in the measurement experiments since soft tissues are in general anisotropic. Generally, it will be too expensive even if it is possible to generate enough data using *in vivo* measurement experiments to obtain adequate statistical interpretation of the mechanical properties of soft tissue. This is primarily due to the extreme technical and ethical demands on such experiments, and vast diversity in mechanical properties of biological tissues.

Indentation tests were used in Davies *et al.*[18] to determine the mechanical properties of spleen tissue. Tie and Desai[19] reported their indentation experiments to characterize the biomechanical properties of porcine liver tissue. Indentation experiment on whole liver organ with inverse finite element parameters estimation was reported in Onodera *et al.*[20] Inverse finite element parameters estimation has increasingly been used in measurement experiments[21] to help determine the mechanical properties of biological tissues. The tissue indentation equipment is generally customary designed and developed by the investigators. In Onodera *et al.*[20] an exponential strain energy function from Fung[22] was implemented into MARC 7 (MSC Software Corporation, USA), a commercially available finite element package popular for nonlinear analysis to perform inverse finite element parameters estimation. However, tissue indentation could be a complex mathematical problem involving both compressive and tensile properties of tissue. If at all possible, it is difficult to separate the compressive and tensile properties of the tissue samples.

Uniaxial load testing has long been used to measure the mechanical properties of both soft and hard tissues.[23] Miller and Chinzei[24] described a uniaxial compression test to measure the mechanical properties of brain tissue. Uniaxial compression and elongation experiments with porcine liver were reported in Chui *et al.*[25] and Sakuma *et al.*[26] Uniaxial load testing is simple but, nevertheless, provides us with basic and useful information on the mechanical properties of liver tissue. There are extensive reports on uniaxial testing with arterial elasticity, e.g. see Ref. 27 and references cited therein. Extensive uniaxial testing with liver tissue is relatively few. The zero stress state of the tissue sample must be identified for testing. However, this identification may not be easy since the neighborhood of the zero stress state of a soft tissue is soft and difficult to handle. The combined compression and elongation test[25,26] enabled the zero stress state to be precisely determined for the tensile test after the compression cycle. The combined compression and elongation cycle was clearly a simpler method compared to other more elaborated approaches for example the use of laser for initial state estimation.[9,24]

2.1. *Preparation of tissue sample*

Careful tissue sample preparation is necessary because cutting the samples possibly affects the results obtained. For example, particular attention should be paid to the orientation of tissue samples because biological tissues are mostly anisotropic, and their mechanical properties depend on direction. In order to determine a mechanical property as close as possible to that of *in vivo*, it is important to test the tissue fresh and maintain its freshness during experiments.

Fresh porcine livers were purchased from a local slaughterhouse for our measurement experiments. Rat liver organs were used in experiments in the "Virtual Rat" project.[28] However, it is generally believed that the mechanical properties of pig liver are close to those of human liver. The weight of a whole porcine liver was 1.5 ± 0.2 kg. The liver was approximately 210 mm by 330 mm with a thickness of 35 mm. Test samples were cylindrical in shape with a fixed diameter of 7 mm and height ranging from 4.5 mm to 11 mm. Figure 2 illustrates the preparation of cylindrical test sample. To establish maximum bonding between the tissue and the attachment unit, we tested the adhesion between liver tissue and various surfaces including wood, steel, cloth and rubber. Adhesion to the rubber plate was maintained with the highest tension used in our experiments. This was twice that obtained using wood, which had the lowest value. At a temperature of 20 ± 3°C, the surgical bond was able to sustain a stress of up to 380 kg/cm.^{2}

Before testing, liver tissue samples were visually inspected for visible vessels and large porous. Samples with vessel or obvious porous were discarded. Since the samples were rather small at 7 mm diameter and generally less than 10 mm in height, and the fact that they were extracted near the liver surface, we were quite certain that the presence of vessel in sample was not significant.

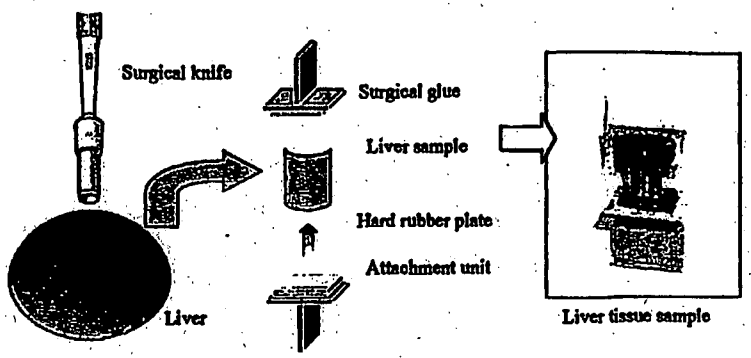

Fig. 2. Overview of cylindrical liver tissue sample preparation:[25] a circular surgical knife is used to extract the tissue sample, and then cut to the desired length using normal surgical knife. Surgical bond (Adhesive A, Sankyo Co. Ltd., Tokyo, Japan) was used to glue the sample to the attachments.

2.2. *Experimental setup*

The test unit was made and placed under a testing machine for experiments. Force and displacement were measured during the loading test by the precision instrument, Eztest, from Shimadzu Co Ltd. of Japan. This instrument had a resolution of ±1%, and could support loading rates ranged from 0.5 to 1000 mm/min. A load cell that was capable of measuring a force up to 20 N was used. A video camera was placed in front of the test sample to record the deformation. The environmental temperature was maintained at about 22°C. Humidity was kept between 60% and 70% to prevent drying of the test pieces.

2.3. *Uniaxial loading tests*

The tests could be classified into following categories: elongation/compression tests, creep tests and relaxation tests. In uniaxial tests, an increasing force is steadily applied to a tissue sample in one direction, and the resulting sample deformation is measured, which gives relations between stress and strain (or stretch ratio). For theoretical treatment, stress and strain in the Lagrangian sense was reference. The tensile or compressive stress T is the load F divided by the cross sectional area A of the sample at zero stress state. The "stretch ratio" or "compression ratio" λ is the ratio of the length or height L of the sample stretched or compressed under the load divided by the initial length L_0 at the zero stress state. Strain ε is the ratio of the displacement $(L - L_0)$ divided by L_0, or $\varepsilon = \lambda + 1$.

Creep and relaxation tests are used for the evaluation of the viscoelasticity or inelastic properties of materials. In the creep tests, tissue sample elongation or compression is measured while a constant static or cyclic force is applied to the sample. In the relaxation test, stress reduction is observed while a tissue sample

is elongated or compressed to a constant length and maintained at that length. Uniaxial tensile or compression testing is the most fundamental method for the determination of the elastic properties of materials, which are evaluated primarily on the basis of stress–strain relations.

In addition to performing the conventional uniaxial elongation and compression tests on liver tissue, force–displacement could be measured during a cycle of compression and elongation. In the combined compression and elongation test, the tissue sample is first compressed and then elongated at the same rate to its stress free position and beyond as illustrated in Fig. 3.

Based on the experimental results, by compressing a cylindrical liver sample of diameter 7 mm by a force of less than 1 N, the tensile test could be started at the zero stress and strain state. Figure 4 compares the measured force–strain data from the elongation only experiments and that of the elongation in the combined

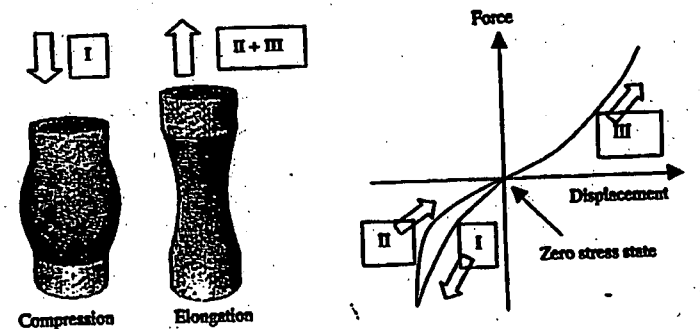

Fig. 3. Illustration of combined compression and elongation test: I — compression phrase; II — return to stress free state; III — elongation phrase.

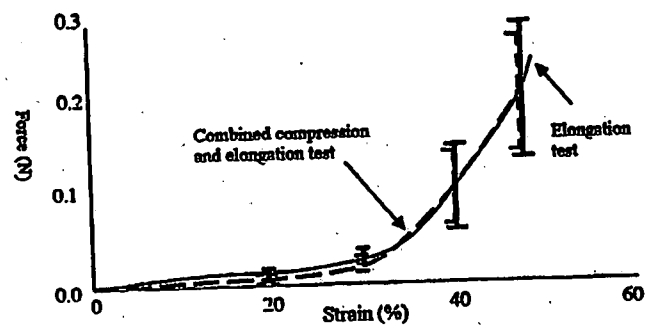

Fig. 4. Comparison of experimental force–strain data from elongation only test and combined compression and elongation test: number of samples = 8, diameter = 7 mm; loading rate = 10 mm/min. Error bar indicates the standard deviation from the average experimental data.

compression and elongation test. The liver tissue samples were compressed up to 0.4 N in the combined compression and elongation test. The measured data between the two experiments are compatible.

3. Characteristics of Liver Tissue

Liver is the second largest organ of the body after the skin. The surface of the liver is covered by a membrane called the visceral peritoneum, also commonly referred to as liver capsule. The liver capsule extends into the substance of liver as highly branched septae. The human liver is comprised of 4 lobes, with the largest two, the right and left lobe, separated by the falciform ligament. The liver lobes are made up of many functional units called lobules. Each hepatic lobule, which is about 1–2 mm in diameter, is a roughly hexagonal arrangement of plates of hepatocytes radiating outward from a central vein in the center. Hepatic lobules are the structural unit of the liver. They are delineated by the connective tissue septae. Detailed description of liver anatomy can be found in Tortora.[29]

3.1. *Stress–strain relationship*

All the liver specimens in our *in vitro* experiment yielded nonlinear stress–strain behavior, having higher distensibility in the low stress range and losing it at progressively higher stresses. Figures 5(a) and 5(b) illustrated typical stress–strain curves of a porcine liver tissue tested in compression and elongation experiments respectively. Each curve could be divided into three parts. In the first part, from O to A (toe region), the load increases exponentially with increasing compression. This is the physiological range in which the tissue normally functions. In the second part, from A to B (linear region), the stress–strain relationship is fairly linear. In the third part, from B to C, the relationship is nonlinear and ends with rupture. B is the yield point. At point C the maximum load is reached, corresponding to the ultimate stress and strain. D is the break point. The slope defined by points A and B is the elastic stiffness from which Young's modulus of liver tissue during compression and elongation are derived respectively if linear elastic model is assumed in computation. Young's modulus or elastic modulus is a measure of the stiffness of a given material. Figure 5(c) shows the average stress–strain curve from combined compression and elongation test of liver tissue samples. The average stress–strain curve is typically used for biomechanical modeling in surgical simulation.

The combined compression and elongation experiments were also performed on kidney and brain tissues. The stress–strain behaviors of liver, kidney and brain tissues are different. Figure 6 compares the average stress–strain data. The brain tissue is significantly softer compared to liver and kidney tissues. Kidney tissue is stiffer than liver tissue.

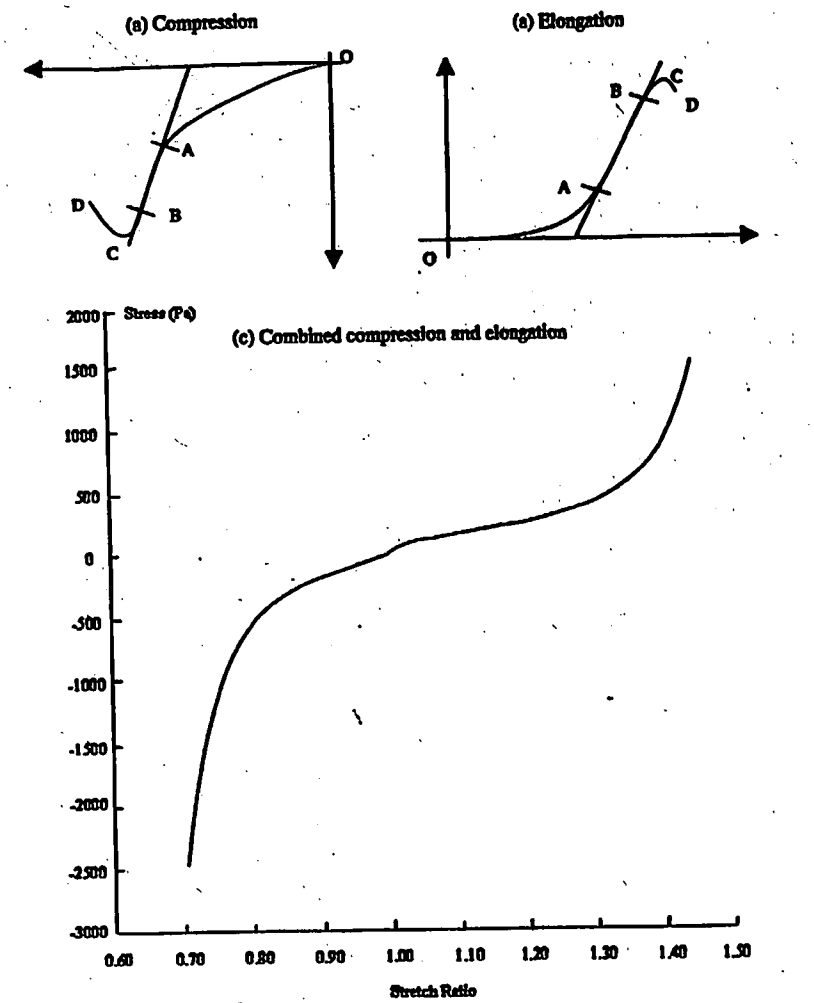

Fig. 5. Typical load–displacement curves of porcine liver tissue until fail during (a) compression and (b) elongation respectively. (c) Average stress–strain curve of combined compression and elongation experiment. Number of samples: 65 from 18 livers. Note that constant loading rate at 10 mm/min is used in all experiments.

3.2. *Nonhomogeneity*

Figure 7 compares the mass density of tissue samples extracted from various parts of a liver organ. Eight groups of samples were extracted from the surface at different locations (A1, A2, B1, B2, C1, C2, D1, D2) in the liver. Mass density is determined

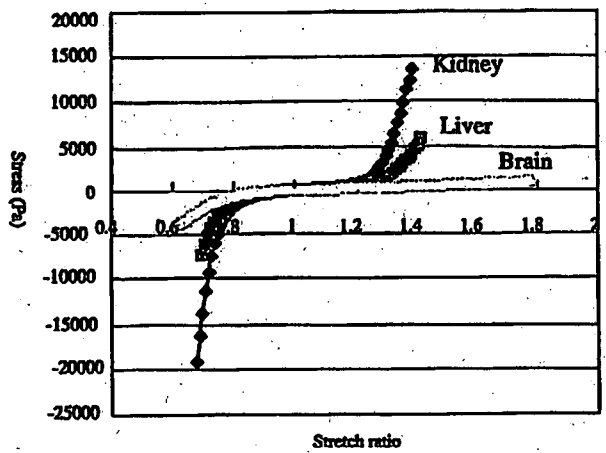

Fig. 6. Comparison of experimental stress–strain data from combined compression and elongation tests of liver, kidney and brain tissues: number of samples = 5 for each tissue type; diameter: 7 mm; loading rate: 10 mm/min.

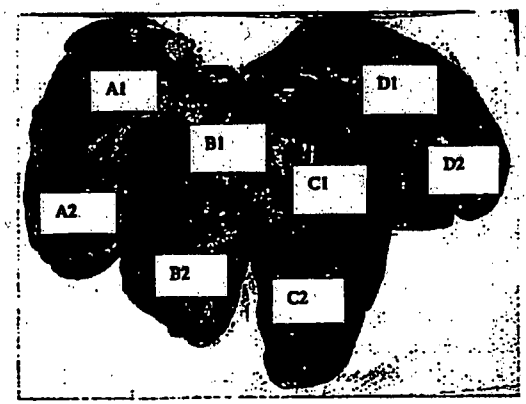

	Density (g/cm³)
A1	1.070
A2	1.078
B1	1.030
B2	1.074
C1	1.058
C2	1.074
D1	1.074
D2	1.057

Fig. 7. Mass densities of tissue samples extracted from different parts of the liver.

by dividing the measured weight by the volume of the tissue sample. There is no apparent different in the stress–strain relationship of these tissue samples in uniaxial loading tests.

From the comparison of the stress–strain curves from visceral side, diaphragmatic side and edge of the liver organs, it was observed that samples extracted from the upper surface (diaphragmatic side) of liver were noticeably harder than those from other parts of the liver. In the experiment,[25] a total of 21

samples were extracted from two porcine livers. Height of the cylindrical samples was about 5 mm. The loading rate was 10 mm/min. The presence of a thin capsular layer on the liver surface may help contribute to the stiffness. Since we were mainly interested in computer aided surgical simulation, with surgical devices such as needles approaching liver from the top, samples extracted from the diaphragmatic side of liver were used in our bio-mechanical analyses of liver properties.

3.3. *Effects of temperature*

The effect of temperature on the mechanical properties of liver is clinically important. Diseased liver organ is heated in RF ablation procedure, and cooled in cryosurgery for cancer cell destruction. Figure 8 compares the stress–strain behavior of liver tissue at different temperature (22°C, 37°C, 60°C and 80°C). The material behavior of liver tissue was essentially the same at 22°C and 37°C. At 60°C, the nonlinear shape of stress–strain curve remains although the tissue is softer. At 80°C, the liver tissue was heat-denatured. This agrees with the observation from Haemunerich *et al.*[30] that water loss from the samples was significant at temperature above 70°C. Haemunerich *et al.* reported an *in vitro* heating of liver samples using two electrodes. In our cooling experiments, we found that freezing has significant effects on the mechanical properties of porcine liver tissue. Chua *et al.*[31] reported an analytical study on the thermal effects of cryosurgery.

The temperature of tissue samples could be maintained with Ringer solution circulated at a constant rate during experiments. Ringer solution is a solution that is isotonic with blood. One liter of ringer solution contains 130 mEq of sodium ion, 109 mEq of choride ion, 28 mEq of lactate, 4 mEq of potassium ion and 3 mEq of calcium ion.

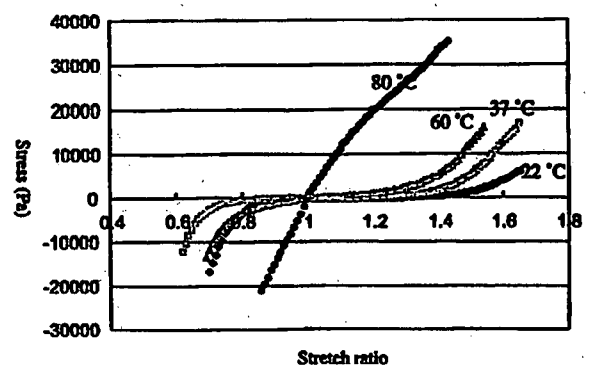

Fig. 8. Comparison of experimental stress–strain data from combined compression and elongation tests of liver tissues at different temperature: number of samples: 12 (3 at each temperature); diameter: 7 mm; loading rate: 10 mm/min.

3.4. *Strain rate dependency*

The effect of strain rate on porcine liver tissue was shown to be relatively insignificant from various experiments (e.g. Refs. 19 and 25). Constant speed of elongation/compression of 1, 2, 5, 10, 20, 50, 100 and 200 mm/min are corresponded to strain rates of 0.003, 0.006 0.030, 0.061, 0.151, 0.303 and 0.606 per second respectively. Varying strain rate has little effect on hysteresis from the stress–strain curves obtained from compression and then elongation testing. Hysteresis is the energy dissipation between the loading and unloading of the tissue during mechanical tests. Figure 9 shows the hysteresis measured during the cycle of compression and elongation to zero stress state in combined compression and elongation experiments with varying loading rates. There is little change in hysteresis when the loading rates range between 5 and 50 mm/min.

As was also reported for other animal tissues,[22] porcine liver exhibited tissue relaxation. During the relaxation experiments, the liver tissue sample was compressed, and then the compression was maintained, the amount of force measured gradually decreased.[26] At low loading rates (1–2 mm/min), some tissue relaxation was observed, while very fast rates (50–200 mm/min) resulted in large increments between data points. Liver tissue is not linear viscoelastic when the loading rates are between 5 and 50 mm/min. The loading rate of 10 mm/min was found to be the most suitable for extensive measurement experiments. This corresponded to a strain rate of between 0.041 per second and 0.015 per second since our samples ranged in height from 4 to 11 mm. This was consistent with values required for our targeted application, that is, computer aided surgical simulation for

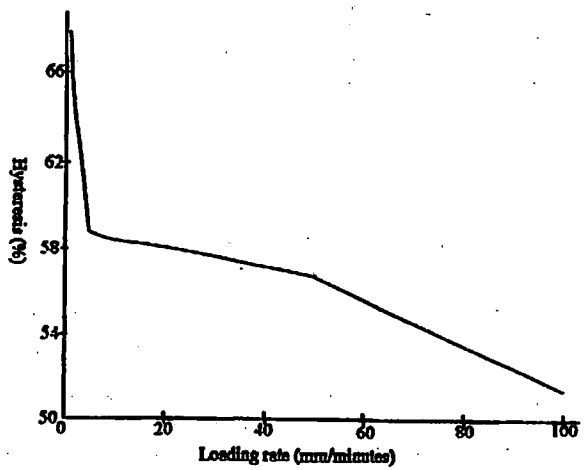

Fig. 9. Strain rate dependency of liver tissue sample: number of samples = 54 from 9 porcine livers; diameter and height of the samples were 7 mm and 5.5–10 mm respectively.

abdominal surgery. Slightly higher strain rates were included in our study because we needed to predict the initial response of liver to a surgical probe. By testing all samples at the same rate, confounding effects of tissue viscoelasticity could be minimized.

3.5. *Incompressibility and Poisson's ratio*

When a solid is subjected to load, it deforms and changes its shape and volume. The volume of an incompressible material remains constant when deform. Biological soft tissues including liver have often been assumed to be incompressible. Liver tissue incompressibility can be studied via measurement of Poisson's ratio. The values of Poisson's ratio for most engineering materials are constant and range between 0.25 and 0.35.

With reference to a cylindrical sample of height H and diameter D under a load τ, elastic elongation or compression in the direction of the applied load (known as axial strain ε_a) is accompanied by contraction or expansion in the perpendicular direction (known as transverse strain ε_t). Poisson's ratio is defined as the negative ratio of transverse strain to axial strain ($\varepsilon_t/\varepsilon_a$). Poisson's ratio is a material property that has received relatively less attention. This parameter is difficult to measure experimentally particularly for biological soft tissue which is generally heterogeneous and anisotropic, in addition to its softness which makes handling difficult.

To determine Poisson's ratio, a digital video camera was used to record the compression and elongation process with force at each instant measured and noted. The video was then processed, and broken into individual frames. Each frame was processed to determine the mean diameter of the tissue samples D, and this value was compared with the previous frame to determine ΔD. The Poisson's ratios during compression and elongation were readily determined since the axial displacement ΔH is known. Figure 10(a) illustrates the experimental setup used to determine the Poisson's ratio of liver tissue, and a typical frame captured using the digital camera was shown in Fig. 10(b).

In theory, Poisson's ratio for a biological material can vary from less than zero to over one half. This is in contrast to the 0–0.5 range for isotropic continua. Consistent with the theory, we have determined that the Poisson's ratio for compression and elongation were 0.466 ± 0.147 and 0.431 ± 0.155 respectively. The values were measured from a size of 15 tissue samples for compression and 24 tissue samples for elongation. Figure 11 compares the Poisson's ratio for compression and elongation.

3.6. *Anisotropy*

Markers on the test sample were prepared and deformation of the sample during experiment was recorded via a digital video camera described above. Figure 12 was snap shots in the middle and end of the tension experiment. We observed that

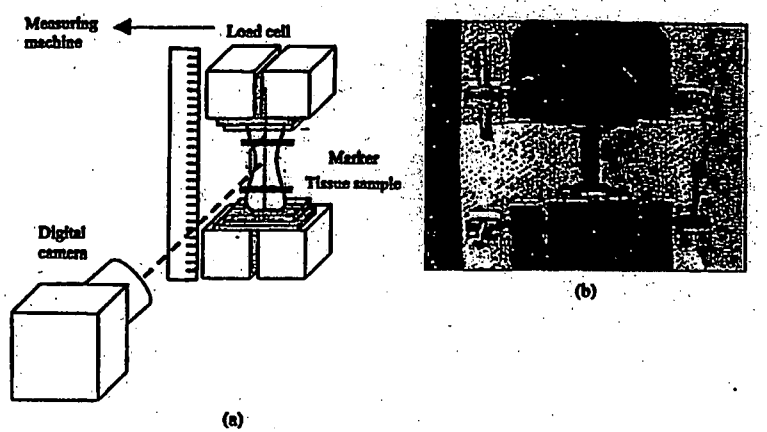

Fig. 10. Overview of experiments to determine Poisson's ratio of porcine liver tissues: (a) experimental setup for Poisson's ratio measurement; (b) snap shot of tissue sample during experiment.

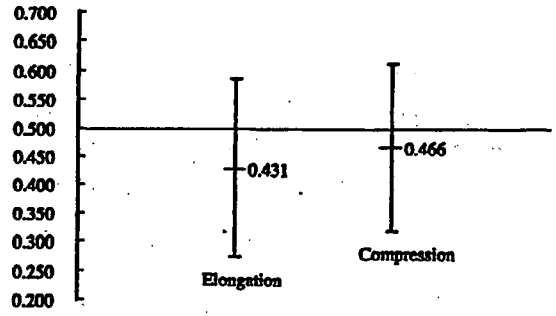

Fig. 11. Comparison of Poisson's ratio during elongation and compression experiments of liver tissue samples. Number of samples: 15 for compression; 24 for elongation.

there was a tendency for liver to displace in the direction of the force, which was acting perpendicular to the cross sectional x–y or horizontal plane. The originally horizontal marker placed on the specimen remained roughly horizontal at the middle and end of elongation. If there is no plane of symmetry or transverse, the marker will fail to remain horizontal. The horizontal displacement from necking differs from the vertical displacement. We did not observe any change in the shape of the cross sectional plane of the sample. The porcine liver tissue sample is likely to be a transversely isotropic material with the principal axis along the z direction or vertical plane. Investigation on the anisotropy properties of porcine liver tissue has been reported in Ref. 74.

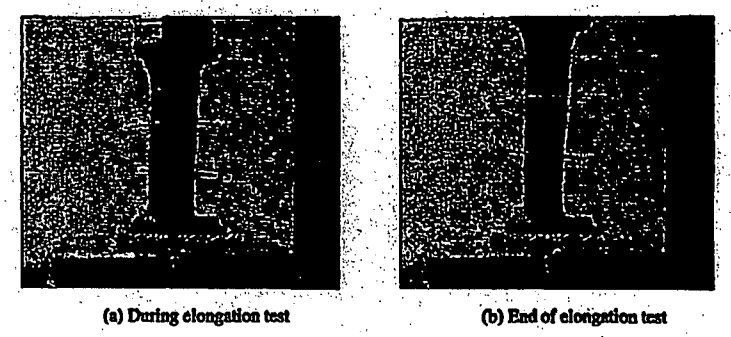

Fig. 12. Snap shots of deformation of liver tissue sample during experiment.

In summary, liver tissue is incompressible and is not isotropic at the length scale of approximately 10 mm. The liver tissue also possesses a nonlinear stress–strain behavior. It is not quite strain rate dependent. Linear viscoelasticity is not significant at moderate strain rate experienced during surgery. The liver tissue samples can be considered as a homogeneous material if they are extracted from the surface of the liver organ. They are noticeably harder than brain tissue and softer than kidney tissue.

4. Strength and Elastic Modulus of Liver Tissues

From investigation on the strength of liver tissue, the yield stress and strain were approximately 2.5×10^5 Pa and 69.5% for compression. With this yield stress, the compressive stress achieved by 1 N was one order of magnitude less than the yield stress. The resultant force–displacement relationship before and after preconditioning was found to have not change with 1 N of preconditioning load. Precondition may not be necessary since surgeon interacts with non preconditioned tissues and/or organ.

Assuming a linear elastic model, we determined that the mean modulus was 1355 kPa with a standard deviation of 0.7811×10^5 Pa. The mean yield stress was $-2.478 \pm 0.7811 \times 10^5$ Pa. The ultimate stress lies in the range of -1364×10^5 to -4.054×10^5 Pa. The maximum compression at rupture was between 61% and 79%. The measured parameters of the 13 *in vitro* destructive compression tests are listed in Table 1.

Determining Young's modulus of the liver tissue during elongation proved to be harder than compared with that of compression. This was due to our experimental method using surgical bond in attaching the specimen to the measuring instrument. As described in Sakuma *et al.*[26] this method had an advantage in stress concentration and possessed no slipping as in conventional uniaxial tests using clamps. However, the bond adhesiveness was weaker compared

Table 1. Material parameters measured from compression of liver specimens. The diameter and height of each specimen was 7 mm and 5 mm respectively. Stress is in terms of 1×10^5 N/m^2 and Young's modulus is in terms of 1×10^6 N/m.^{2}

Specimen	Yield		Maximum		Break		Young's modulus
	Stress	Strain (%)	Stress	Strain (%)	Stress	Strain (%)	
1	−3.118	−71	−3.352	−74	−3.066	−76	1.299
2	−3.637	−71	−3.767	−73	−3.611	−75	2.055
3	−3.118	−73	−3.507	−75	−3.170	−76	1.359
4	−2.910	−69	−3.144	−72	−2.858	−74	1.336
5	−1.948	−72	−2.104	−74	−1.974	−75	1.006
6	−2.468	−75	−2.754	−77	−2.442	−79	1.862
7	−1.922	−72	−2.130	−74	−1.689	−75	1.380
8	−2.546	−75	−2.754	−77	−2.598	−78	1.110
9	−2.468	−75	−2.754	−77	−2.442	−79	1.862
10	−3.637	−71	−4.053	−74	—	—	1.707
11	−1.546	−59	−1.689	−61	—	—	0.707
12	−1.533	−58	−1.611	−60.5	−1.585	−61	0.890
13	−1.351	−63	−1.364	−64	−1.039	−70	1.039
Mean	−2.478	−69.54	−2.691	−71.82	−2.313	−74.36	1.355
Standard deviation	0.781	5.825	0.862	5.988	0.805	5.104	0.413
Range	(−1.351, −3.638)	(58, 75)	(−1.364, −4.054)	(60.5, 77.4)	(−1.039, −3.612)	(61, 79)	(0.707, 2.055)

to the liver tissue. The attachment gave way prior to the break point of the liver tissue during elongation. In order to overcome this problem, separate tests using clamps were conducted to measure the ultimate stress and strain. The measured material parameters of all the seven tests are listed in Table 2. We determined that the mean value of ultimate stress and ultimate strain were 6.9×10^4 Pa and 79% respectively. Young's modulus was 227 kPa. This is significantly smaller than that determined during compression.

For comparison, liver tissue was stiffer than the muscular tissue and somewhat close to artery tissue. The artery tissue can withstand a larger strain compared to that of liver tissue. It was reported in the literature that Young's modulus, maximum stress and strain of artery were 200 kPa, 2×10^6 N/m^2 and 100% respectively during elongation. For muscular tissue, the corresponding values were 30 kPa, 2×10^5 N/m^2 and 60%.

Note that engineering stress and strain were referenced in the above discussions. For comparison, Young's modulus was measured from true stress and true strain during elongation experiments. The Young's modulus ranged from 500 to 750 kPa. This was consistent with the value of 650 kPa from experiments by Toyota Co, Japan reported in Chui *et al.*[31] It was typical for Young's modulus calculated from

Table 2. Material parameters measured from elongation of liver specimens. Height is between 7 and 9.5 mm, stress is in 1×10^4 N/m,^{2} and Young's modulus is in 1×10^5 N/m.^{2} All specimens have the same initial cross sectional area with diameter = 0.007 m.

Specimen	Yield		Maximum		Young's modulus
	Stress	Strain (%)	Stress	Strain (%)	
1	4.9	68.89	6.756	86.67	2.046
2	4.9	68.75	5.847	86.25	2.161
3	2.9	71.76	3.378	77.06	1.822
4	5.8	59.50	7.2	68.0	2.620
5	8.4	70.00	10.0	82.0	2.695
6	8.0	60.00	8.6	65.0	2.857
7	5.8	82.00	6.7	88.0	1.727
Mean	5.826	68.7	6.926	79.0	2.276
Standard deviation	1.89	7.61	2.088	9.32	0.448
Range	(2.91, 8.4)	(59.5, 82)	(3.378, 10.0)	(65.0, 88.0)	(1.727, 2.857)

true stress to be higher than that calculated using engineering stress. Nevertheless, the different was significant.

5. Mathematical Description of Liver Tissue Elasticity

A constitutive equation describes a physical property of a material. Its derivation should begin with empirical measurements. There are two alternatives for constitutive modeling: the continuum approach and the microstructure approach. With the first approach, the material is assumed to be a continuum. The relevant variables are identified, and these are related in a framework that ensures invariance under a change of frames. This was our approach in this paper.

One of the earliest reported mathematical/experimental treatments of biologic materials in the context of large deformation and modern continuum mechanics was that of Ticker and Sacks, 1964 and 1967, according to Vossoughi.[33] Since then, a number of constitutive models have appeared that described the passive material properties of both hard and soft tissues. However, few deal with abdominal tissues such as the liver. If the material is linear and the deformation is limited and infinitesimal, then a simple linear relationship derived according to Hooke's law might be sufficient to uniquely describe the stress-strain relationship. The formulation is not unique for a nonlinear material capable of undergoing large deformations. One constitutive model may well represent one type of soft tissue but not the others, or a model may well approximate a portion of the stress-strain curve, but not the entire space. The numerical complexity of these nonlinear functions is also an issue for interactive computing using currently available computer hardware and software.

In Carter *et al.*[13] and Davies *et al.*[18,34] the authors described biomechanical modeling with experimental indentations of animal abdominal organs, including liver. Their study assumed that the tissues were isotropic, homogeneous and incompressible. A nonlinear constitutive model based on a strain energy polynomial function was used in Miller[35] to model liver and kidney, using experimental results from *in vivo* experiments on Rhesus monkeys by Melvin *et al.*[36] The experiments approximated uniaxial compression under high strain rates typical for car crashes. These nonlinear models were numerically complex, and not suitable for fast medical simulation.

A well-known approach for studying nonlinear constitutive relations of bodies capable of finite deformation is to postulate that elasticity has the form of an elastic potential, or strain energy function, W. A number of constitutive models based on strain energy have already been proposed to describe the passive material properties of soft tissues. For solid biomechanics, most of the work has concentrated on blood vessels and myocardium. There are fewer reports of work on lung, skin, ligament, tendon, cartilage and bone tissue. Chui *et al.*[25] reports strain energy based constitutive relation that is derived from extensive measurements on liver tissue samples. There are also some recent reports on empirical expressions for fitting uniaxial tensile stress–strain relationship of soft tissue. These expressions are generally computational efficient and do not reduce to the form of strain energy. We tried to determine a constitutive equation that could fit the experimental data. The theoretical curve should follow the shape of the average curve with small standard error. Standard error is defined as root means square errors (RMSE), and is calculated from the difference between the theoretical estimate and the experimental measurement. To estimate the coefficients for the nonlinear functions, software for nonlinear least-square data fitting using the Gauss–Newton method could be used. Generally, models with few material parameters are preferred for the purpose of computational efficiency. Numerical stability of the parameters is desired for finite element computation. Depending on the specific applications, the constitutive model used is a trade off between computational accuracy and interactivity. Stress–strain graphs of compression, elongation and combined compression and elongation experiments can be found in Chui *et al.*[25]

5.1. *Empirical expressions*

The most popular expression that is not reduced to the form of strain energy is the exponential function by Tanaka and Fung.[37,38] Tanaka and Fung proposed a constitutive relation for soft tissue for simple uniaxial state of stress–strain as:

$$\sigma = (\sigma^* + \beta)e^{C_1(\lambda-\lambda^*)} - C_2$$

where σ and λ are the stress and stretch ratio, $\sigma*$ and $\lambda*$ corresponds to a point on the stress–strain curve, C_1 and C_2 are the material constants. A variant from

Fung[22] with an additional material constant is,

$$T = C_1 e^{C_2\lambda} - C_3$$

where T is the engineering stress, C_1, C_2 and C_3 are the material constants. The other empirical formulae proposed to fit experimental stress–strain data include Kenedi *et al.*[39] and Ridge and Wright.[40] The former with two material constants is,

$$T = C_1\lambda^{C_2-1} - \frac{1}{\lambda}.$$

The empirical formulae are simple. However, they are limited to a uniaxial state of stress–strain. These equations could model the stress–strain curve of elongation reasonably well. Generally, they do not fit the experimental data on compression of liver tissues well. All of these equations could not model the stress–strain curve from combined compression and elongation experiments. A more general multi-axial based formulation is preferred for medical simulation.

5.2. *Strain energy functions*

The strain energy for an elastic body is a function of the state of deformation. Let $\mathbf{X}$ denotes a point in the reference configuration. The current position of the point is denoted by $\mathbf{x}$, where $\mathbf{x}$ is a function of time. The gradient of $\mathbf{x}$ with respect to $\mathbf{X}$ is called the deformation gradient,

$$\mathbf{F} = \left(\frac{\partial \mathbf{x}}{\partial \mathbf{X}}\right)^T.$$

The right Cauchy–Green tensor, $\mathbf{C}$ is a measure of the strain the body experiences and is given by

$$\mathbf{C} = \mathbf{F}^T\mathbf{F}.$$

The constitutive assumption of nonlinear elasticity is that the stress tensor at point $\mathbf{x}$ depends only on the material and the deformation gradient at $\mathbf{x}$. If the mechanical properties do not depend explicitly on the particular point $\mathbf{x}$, the material is said to be homogeneous. The liver tissue is assumed to be homogeneous and incompressible in this investigation.

When a quantity is unchanged with a frame rotation, it is said to be invariant. From $\mathbf{C}$, which is a second order tensor, three scalar invariants can be formed by taking the trace of $\mathbf{C}$, $\mathbf{C}^2$ and $\mathbf{C}^3$. They are

$$I = \text{trace}(\mathbf{C}) = C_{ii},\ II = \text{trace}(\mathbf{C}^2) = C_{ij}C_{ji} \text{ and } III = \text{trace}(\mathbf{C}^3) = C_{ij}C_{jk}C_{ki}.$$

However, it is customary to use strain invariants

$$I_1 = I,\quad I_2 = \frac{1}{2}(I^2 - II) \text{ and } I_3 = \frac{1}{6}(I^3 - 3I\cdot II + 2III) = \det(\mathbf{C}).$$

Assuming that liver tissue is isotropic, the strain energy function can be expressed as a function of the above strain invariants, $W(I_1, I_2, I_3)$. We denote λ_i as the principal values of $\mathbf{F}$ and I_i is a function of λ_i.

$$\mathbf{F} = \begin{pmatrix} \lambda_1 & & \\ & \lambda_2 & \\ & & \lambda_3 \end{pmatrix}$$

Since liver is known to comprise highly incompressible material, $\det \mathbf{F} = \lambda_1\lambda_2\lambda_3 = 1$. Under uniaxial deformation, the cross-sectional area of the cylindrical sample reduces by $1/\lambda$ when the height of the sample is increased by a factor of λ. By setting $\lambda = \lambda_3$, we have $\lambda_1 = \lambda_2 = \frac{1}{\sqrt{\lambda_3}}$. Invariants I_1, I_2 and I_3 under uniaxial deformation can be evaluated as $I_1 = \lambda^2 + 2/\lambda$, $I_2 = 2\lambda + 1/\lambda^2$ and $I_3 = 1$, respectively.

For an elastic material, the second Piola-Kirchhoff stress tensor $\mathbf{S}$ can be expressed in terms of strain energy W and Green–Lagrange strain tensor $\mathbf{E}$ as

$$\mathbf{S} = \frac{\partial W}{\partial \mathbf{E}} = 2\frac{\partial W}{\partial \mathbf{C}}.$$

The Cauchy stress σ is related to $\mathbf{S}$ by

$$\sigma = \frac{1}{J}\mathbf{F}\cdot\mathbf{S}\cdot\mathbf{F}^T$$

where $J = \det \mathbf{F}$. Component of σ in the tensile or compressive direction could now be expressed as partial derivative of W by the invariants.

$$\sigma = 2\frac{\partial W}{\partial I_1}\left(\lambda^2 - \frac{1}{\lambda}\right) + 2\frac{\partial W}{\partial I_2}\left(\lambda - \frac{1}{\lambda^2}\right). \tag{1}$$

Cauchy stress σ is related to the first Piola-Kirchhoff stress tensor $\mathbf{T}$ by

$$\sigma = \frac{1}{J}\mathbf{F}\cdot\mathbf{T}.$$

Since $\sigma = \lambda T$, we can deduce from Eq. (1) that

$$T = \frac{2}{\lambda}\frac{\partial W}{\partial I_1}\left(\lambda^2 - \frac{1}{\lambda}\right) + \frac{2}{\lambda}\frac{\partial W}{\partial I_2}\left(\lambda - \frac{1}{\lambda^2}\right). \tag{2}$$

Suppose that the original cross sectional area of the cylindrical sample used in our experiment is A_0 and the tensile or compressive load is F,

$$T = \frac{F}{A_0}.$$

Suppose that the original length of the cylindrical sample is L_0, the displacement is $\Delta L = L_0(\lambda - 1)$.

T and ΔL are concurrently measured in the experiments. By comparing the experimental curve obtained by plotting T against λ with the theoretical curve from Eq. (2) obtained using various strain energy functions, the strain energy function that can best represent the material behavior of porcine liver tissue could

be determined. For example, with the following Mooney–Rivlin energy function with nine material constants (known as the 9-constant theory),[43]

$$\begin{aligned} W = {} & C_1(I_1 - 3) + C_2(I_2 - 3) + C_3(I_3 - 3)^2 + C_4(I_1 - 3)(I_2 - 3) \\ & + C_5(I_2 - 3)^2 + C_6(I_1 - 3)^3 + C_7(I_1 - 3)^2(I_2 - 3) \\ & + C_8(I_1 - 3)(I_2 - 3)^2 + C_9(I_2 - 3)^3 \end{aligned}$$

where C_1, C_2, C_3, C_4, C_5, C_6, C_7, C_8 and C_9 are material constants. The stress–strain relationship could be derived by substituting W into Eq. (2). The resulting equation was highly complex, with the highest order term having a power of 6 and the lowest order term having a power of −5.

Equation (3) is the 2-constant version of the energy function for the Mooney–Rivlin material.

$$W = \frac{C_1}{2}(I_1 - 3) + \frac{C_2}{2}(I_2 - 3) \tag{3}$$

where C_1 and C_2 are material constants and C_1, $C_2 > 0$. Similarly, partial differentiation of W, with I_1 and I_2 obtained from Eq. (2) yielded the following stress–strain relation.

$$T = C_1\lambda + C_2 - \frac{C_1}{\lambda^2} - \frac{C_2}{\lambda^3}$$

whereλ is equal to strain plus one. For ease of discussion, we simply refer to $T = f(\lambda)$ as stress–strain relation. How well this stress–strain relation represented the experimental data could be evaluated using this stress–strain relation. Our assumption on isotropic, homogeneous and incompressible liver model is consistent with recent literature[13,18,35,41,42] on modeling of abdominal organs for surgical simulation.

There are several types of strain energy functions: polynomial, exponential, logarithmic and power. The Mooney–Rivlin material is an example of a strain energy function with polynomial form. The simplest polynomial-based energy function is the neo-Hookean model, which was originally applied to incompressible nonlinear elastic engineering materials. The neo-Hookean model is a subset of the Mooney–Rivlin model with $C_2 = 0$. There is only one material constant C_1 in this equation shown below:

$$W = C_1(I_1 - 3).$$

An exponential form of strain energy due to Fung[38] and Demiray[54] is shown as follows,

$$W = \frac{C_1}{2C_2}(e^{C_2(I_1-3)} - 1)$$

where C_1 and C_2 are material constants, and $C_1, C_2 > 0$.

Other exponential strain energy function includes Veronda and Westmann[44] shown as follows,

$$W = C_1(e^{C_3(I_1-3)} - 1) + C_2(I_2 - 3) + g(I_3).$$

If liver tissue is assumed as incompressible, $g(I_3) = 0$.

A related class of exponential equations with logarithmic form was proposed by Hayashi and Takamizawa.[45,46] The equation was intended for transversely anisotropic material:

$$W = -C_1 \ln\left(1 - \frac{1}{2}C_2(I_1 - 3)^2 + \frac{1}{2}C_3(I_4 - 1)^2 + C_4(I_1 - 3)(I_4 - 1)\right).$$

The corresponding logarithmic equation for isotropic material is as follows,

$$W = -C_1 \ln(1 - C_2(I_1 - 3)).$$

The main difference between isotropic version and the original Hayashi equation is the absent of invariant I_4 in the former. This invariant was not applicable with an isotropic material.

The fourth type of commonly used constitutive relation is the power law of the form $T = KS^n$ where T is the Lagrangian stress tensor, S is the strain or strain rate tensor, and K and n are the material constants. The advantage of power law stress–strain function is its simplicity. The following equation originally proposed by Tanaka and Fung[37] was used to model the zero-stress state of blood vessel walls in Xie *et al.*[47]

$$T = C_1(\lambda - 1)^{C_2}.$$

Other applications of the power law energy function include the formulation of extrafibrillar matrix of tendor material as a hyperelastic material using Odgen form of strain energy function[49] expressed by,

$$W = \sum_{n=1}^{3} \frac{C_n}{\alpha_n}(\lambda_1^{0.5\alpha_n} + \lambda_2^{0.5\alpha_n} + \lambda_3^{0.5\alpha_n}),$$

$$T = \sum_{n-1}^{3} \frac{C_n}{2}(\lambda^{\alpha_n} - \lambda^{0.5\alpha_n - 1}).$$

A variant of Odgen model was proposed in Bogen *et al.*[50] to describe passive myocardial behavior, where C_1 and C_2 are material constants. The equations were as follows,

$$W = \frac{C_1}{C_2}(\lambda_1^{C_2} + \lambda_2^{C_2} + \lambda_3^{C_2} - 1),$$

$$\sigma = C_1(\lambda^{C_2} + \lambda^{-2C_2}).$$

The corresponding first Piola-Kirchhoff form of Bogen equation is

$$T = C_1(\lambda^{C_2 - 1} + \lambda^{-2C_2 - 1}).$$

The combined logarithmic and polynomial model[25] can be derived in the same spirit as the derivation of combined exponential and polynomial model in Fung *et al.*[51] At low strain, the logarithmic component in the combined model was small, and the polynomial component was the dominant one. Their roles were reversed at high strain. The combined logarithmic and polynomial model is therefore advantageous in describing the entire stress–strain curve. Note that the Veronda and Westmann model also has both exponential and polynomial terms. The Veronda and Westmann model was a sum of an exponential function and a polynomial originally for constitutive modeling of the skin. The combined logarithmic and polynomial equation for isotropic materials is as follows,

$$W = \frac{-C_1}{2}\ln(1 - C_2(I_1 - 3)) + C_3(I_1 - 3).$$

To simplify the discussion, we referred to this equation as the combined logarithmic and polynomial model or combined energy model.

Almost all the constitutive models provided good fits for the experimental data over the elongation region. The fits for the neo-Hookean and the Mooney–Rivlin (2-constants) were not acceptable for the purpose of fitting the entire curves. Not all equations provided good fits for the experimental compression data. The Tanaka model could not match the compression stress–strain curve since a power equation could not represent compression since the theoretical stress computed using this equation was always positive for all positive stretch ratios. Failure of these equations to match the experimental data of combined compression and elongation test was partly due the difficulties in representing both negative and positive domains numerically. A RMSE of greater than 120 Pa is considered a bad fit. The combined energy model and Mooney–Rivlin (9-constant) model were the only models that could adequately represent these data.

The best constitutive model appeared to be the combined logarithmic and polynomial equation.[26] The combined energy equation provided a good fit for the stress–strain relationships in the tests involving compression followed by elongation, as well as consistently matching the independent compression and elongation data. Although the combined model has larger RMSE than that of Mooney–Rivlin (9-constant, the former has smaller number of material constants and the parameters are numerically more stable. With Mooney–Rivlin (9-constant) model, the material parameters varied widely — a parameter could be positive in one